# A Precursor-Limited Nanoparticle Coalescence Pathway for Tuning the Thickness of Laterally-Uniform Colloidal Nanosheets: The Case of SnSe

**Dimitri D. Vaughn II, Su-Il In, and Raymond E. Schaak***

Department of Chemistry and Materials Research Institute, The Pennsylvania State University, University Park, Pennsylvania 16802, United States

**ABSTRACT** The availability of high-quality colloidal nanosheets underpins a diverse range of applications and investigations into dimension-dependent physical properties. To facilitate this, synthetic methods that yield single-crystal colloidal nanosheets with regular shapes, uniform lateral dimensions, and tunable thicknesses are critically important. Most strategies that yield colloidal nanosheets achieve some, but not all, of these morphological characteristics. Here, we describe a synthetic pathway that generates colloidal nanosheets of SnSe with uniform lateral dimensions and tunable thicknesses. SnSe represents an excellent prototype system for studying the formation of colloidal nanosheets because of its layered crystal structure and the growing interest in its potential application as an absorption layer in low-cost photovoltaic devices. Freestanding colloidal SnSe nanosheets were synthesized by slowly heating a one-pot reaction mixture of $SnCl_2$, oleylamine, trioctylphosphine selenide (TOP-Se), and hexamethyldisilazane (HMDS) to 240 °C. The SnSe nanostructures adopt a uniform square-like morphology with lateral dimensions of approximately 500 nm × 500 nm, and the average nanosheet thicknesses can be tuned from approximately 10 to 40 nm by adjusting the concentrations of the $SnCl_2$ and TOP-Se reagents. Aliquot studies reveal fundamental insights into how the nanosheets form: they first "grow out" laterally *via* coalescence of individual nanoparticle building blocks to yield a single-crystal nanosheet template and then "grow up" vertically (through nanoparticle attachment to the nanosheet template) in a pseudo layer-by-layer fashion. Vertical growth is therefore limited, and can be controlled, by reagent concentration. Drop-cast films of the SnSe nanosheets are photoactive and have a bandgap of approximately 1 eV. These studies, demonstrated for SnSe but potentially applicable to other systems, establish a straightforward pathway for tuning the thicknesses of colloidal nanosheets while maintaining lateral uniformity.

**KEYWORDS:** colloidal nanosheets · nanoparticle synthesis · nanoparticle coalescence · reaction pathway studies · narrow bandgap semiconductors · tin selenide (SnSe)

Colloidal nanosheets comprise an important class of two-dimensional crystals that underpin a large number of diverse applications.[1−4] For example, colloidal nanosheets serve as building blocks that facilitate the construction of thin film, composite, and multilayer architectures for applications that include batteries,[5] solar cells,[6,7] catalysts,[8,9] and structurally reinforced polymers.[10,11] Multicomponent nanosheet assemblies couple semiconductors, catalysts, magnets, and plasmonic nanoparticles for multifunctional applications such as magnetically alignable optical crystals[12,13] and photocatalytic water splitting architectures.[14,15] Colloidal nanosheets also permit fundamental studies of dimension-dependent physical phenomena, which can lead to new and unanticipated properties and applications. A recent example of this is graphene, where the two-dimensional nanosheet structure directly underpins its unique electronic properties and its diverse applications.[4,16] A large number of chalcogenide and oxide nanosheets have been used to probe dimension-dependent optical,[17−20] electrical,[21−23] magnetic,[24,25] and superconducting[26] properties, and they have also been exploited in a diverse range of applications that include solar energy conversion,[27] Li ion batteries,[5,28,29] and dielectric films.[22] For these reasons, controlling the characteristic features of colloidal nanosheets—their edge dimensions, lateral uniformity, and thicknesses—is critically important.

The most common synthetic routes to colloidal nanosheets include exfoliation of layered solids,[1,2,21] direct chemical synthesis using colloidal and solvothermal methods,[30−36] and two-dimensional oriented attachment of colloidal nanocrystals.[37−40] Exfoliation strategies, which typically involve the intercalation and subsequent delamination of two-dimensionally bonded bulk crystallites, generally yield single- or multilayer colloidal nanosheets with irregularly faceted edges and nonuniform lateral dimensions that range from less than 100 nm to greater than 1 μm.[21] Colloidal routes can produce nanosheets directly in solution, typically for compounds that adopt layered crystal structures. This is accomplished by using surface

* Address correspondence to schaak@chem.psu.edu.

Received for review August 8, 2011 and accepted September 29, 2011.

**Published online October 12, 2011**
10.1021/nn203009v

stabilizing ligands that permit lateral growth while truncating vertical growth along the stacking axis of the crystal.[31] Colloidal nanosheets have been synthesized by such direct chemical synthesis methods in a diverse range of materials systems, including CdSe,[32] FeSe,[33] $ZrS_2$,[34] Pd,[35] and $WS_2$.[36] Materials that do not have a layered crystal structure often have no intrinsic driving force for 2D anisotropic growth. In these cases, colloidal nanosheets sometimes form *via* the 2D oriented attachment of preformed nanocrystal building blocks;[41−43] representative examples include CdTe,[38] PbS,[39] and $CeO_2$.[40]

Tin selenide, SnSe, is an attractive model system for studying the formation of colloidal nanosheets.[44−54] SnSe adopts a layered GeS-type crystal structure that facilitates two-dimensional growth.[44] As part of a larger family of IV−VI semiconductors that includes SnS,[55−57] GeS,[58] and GeSe,[59] SnSe is also emerging as an important narrow bandgap semiconductor that is of interest as a light absorption layer in solution-processed solar cells and near-infrared optoelectronic devices.[45] It has a large absorption coefficient and a bandgap that overlaps well with the solar spectrum.[46,47] SnSe is also viewed as a less toxic and more environmentally responsible alternative to related narrow bandgap nanoparticles that contain lead or cadmium.[45] Colloidal nanostructures of narrow bandgap semiconductors, including SnSe, can be solution processed using relatively simple methods that include drop casting, spin coating, and inkjet printing.[60] This can facilitate inexpensive fabrication of cheap optoelectronic devices and also permit deposition onto flexible substrates.[61] For SnSe, quasi-spherical and irregularly shaped colloidal nanoparticles have been reported, but rigorous morphological control is rare.[48−50]

Here, we report the direct one-pot chemical synthesis of colloidal SnSe nanosheets with average dimensions on the order of 500 nm × 500 nm and with thicknesses that are tunable between approximately 10 and 40 nm. In addition to being a rare example of uniform single-crystal nanosheets in this size range, we also provide important insights into how the nanosheets form and how their thicknesses can be tuned while maintaining lateral uniformity. To our knowledge, a unified synthetic strategy that permits systematic tuning of colloidal nanosheet thickness has not been demonstrated previously. Such capabilities are important for effectively utilizing two-dimensional nanostructures in applications that include catalysis,[3,15] optoelectronics,[2,4] and spintronics,[16,21] and it also underpins our ability to fully probe and understand quantum size effects in two-dimensional nanostructures. Our findings also help to merge the oriented attachment and surfactant-mediated strategies for nanosheet formation and provide guidelines for controlling the synthesis of large two-dimensional colloidal nanostructures. The colloidal SnSe nanosheets are photoactive and have bandgaps near ~1.0 eV, which is close to the ideal energy for maximum absorption of incident solar radiation.

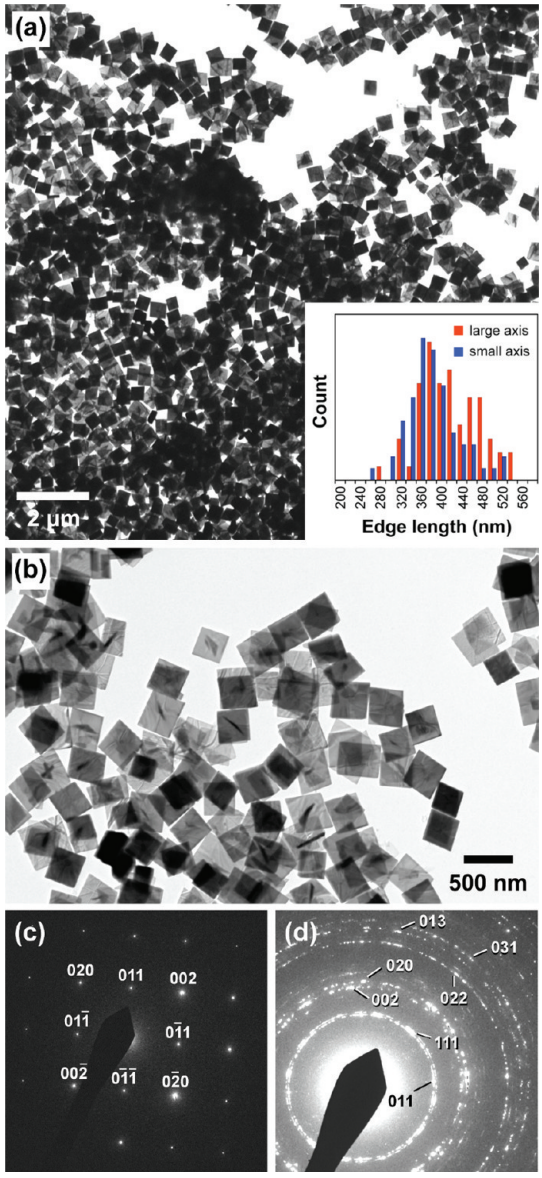


**Figure 1. (a) Large-area TEM image of SnSe nanosheets with corresponding size distribution histogram (inset), (b) higher-magnification image highlighting the uniform square-like morphology, and electron diffraction patterns of (c) a single nanosheet and (d) an ensemble of sheets.**

## RESULTS AND DISCUSSION

**Synthesis of Colloidal SnSe Nanosheets.** Colloidal SnSe nanosheets were synthesized by slowly heating a one-pot reaction mixture of $SnCl_2$, oleylamine, TOP-Se, and HMDS to 240 °C and holding for 30 min. Representative transmission electron microscopy (TEM) images of the SnSe nanosheets, formed using 40 mg of $SnCl_2$, are shown in Figure 1, panels a and b. The nanosheets form as highly uniform square-like structures, and this

morphology persists throughout the bulk of the sample. Several larger-area TEM images are also shown in the Supporting Information (Figure S1). A corresponding size distribution histogram (inset to Figure 1a) shows that the average largest-edge length is 422 ± 63 nm and the average smallest-edge length is 386 ± 57 nm. The electron diffraction pattern taken from an individual nanosheet (Figure 1c) shows a spot pattern that is consistent with a single-crystal nanosheet having its surface normal oriented along the [100] direction. The electron diffraction pattern in Figure 1d was taken from an ensemble of nanosheets, and the polycrystalline ring pattern corresponds to the GeS-type structure of SnSe, with no additional crystalline impurity phases evident.

Energy-dispersive spectroscopy (EDS) analysis also confirms an approximate 1:1 ratio of Sn:Se, within the error range of the technique (Figure 2a). Figure 2b shows powder X-ray diffraction (XRD) data for a drop-cast film and an aggregated powder sample of the SnSe nanosheets. The powder XRD pattern for the aggregated powder sample matches well with that of the simulated pattern for orthorhombic GeS-type SnSe with no observable crystalline impurities. Lattice constants, calculated from the XRD pattern shown in Figure 2b, are $a = 11.47(8)$ Å ($a_{lit} = 11.50$ Å), $b = 4.12(5)$ Å ($a_{lit} = 4.15$ Å), and $c = 4.45(1)$ Å ($c_{lit} = 4.44$ Å).[62] For the drop-cast films of SnSe nanosheets, significant preferred orientation is observed, which confirms that the nanosheet morphology comprises the bulk of the sample. The predominant peaks are (400) and (800), which is consistent with a highly textured [100]-oriented film and is also in agreement with the [100] single-sheet orientation observed by selected area electron diffraction (SAED) in Figure 1c.

Figure 3a shows three TEM images, at increasing levels of magnification, for nanosheets that were found stacked together to reveal a side-on view. The right-hand inset to Figure 3a reveals a stacked structure of nanosheets with thicknesses that range from approximately 35 to 60 nm. (As will be shown below, this sample has the largest average thickness.) Zooming in on a corner of a single nanosheet, the high-resolution transmission electron microscope (HRTEM) image in the main panel of Figure 3a shows a highly crystalline lamellar structure. The left-hand inset to Figure 3a shows an enlarged region of the HRTEM image in the main panel, which highlights the double-layered crystal structure that is characteristic of GeS-type SnSe:[44] alternating layers with interatomic distances of 2.9 and 3.2 Å across the layers (Figure 3b). Comparing the HRTEM image (Figure 3a) with the crystal structure of SnSe (Figure 3b) and the electron diffraction pattern of a single nanosheet (Figure 1c) confirms that the nanosheets are composed of SnSe layers that are oriented with the surface normal along the [100] direction. Further confirmation of this crystallographic orientation

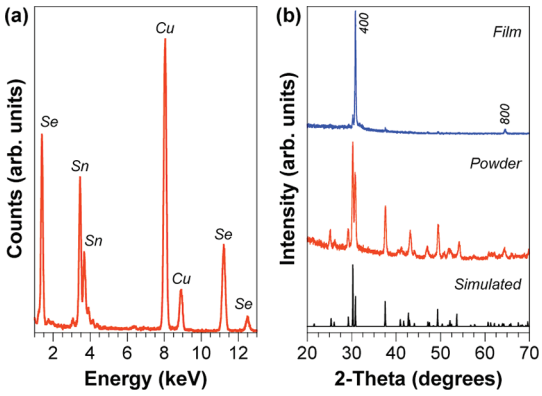


**Figure 2. EDS spectrum and powder XRD patterns for SnSe nanosheets. The EDS spectrum (a) confirms the presence of Sn/Se in an approximate 1:1 ratio, and the XRD pattern (b) confirms that the nanosheets correspond to orthorhombic GeS-type SnSe with preferred orientation in the [100] direction for drop-cast films.**

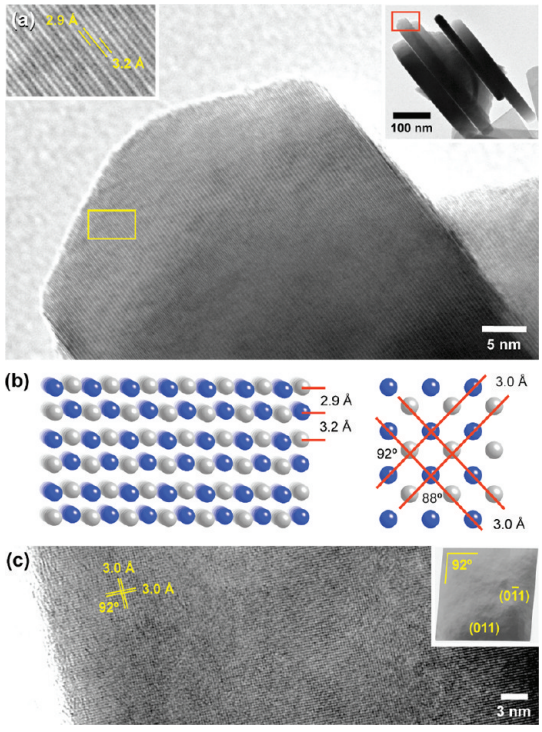


**Figure 3. HRTEM images of SnSe nanosheets and correlation with the crystal structure: (a) three magnifications showing a side view of stacked nanosheets, revealing the SnSe layers that comprise the nanosheets, (b) crystal structure of orthorhombic GeS-type SnSe showing the atomic arrangement and key interatomic distances and angles of the {100} and {011} set of planes, and (c) high- and low-magnification images showing the top view of an individual nanosheet.**

comes from a top-down HRTEM image of a single nanosheet (Figure 3c), which reveals lattice spacings of 3.0 and 3.0 Å and an intersection angle of approximately 92°, which is consistent with the {011} set of planes. This indicates that the nanosheets are bound by {011} facets. Consistent with this, the corners of the nanosheets do not form 90° angles, but rather

92° and 88° angles defined by the intersection of the {011} planes (Figure 3c, inset).

**Tuning the Nanosheet Thickness.** Figure 4 shows representative TEM and AFM images, along with AFM line profile scans, for SnSe nanosheet samples prepared using 40, 20, 15, and 10 mg of $SnCl_2$ with all other reaction conditions remaining constant (except for an analogous decrease in TOP-Se concentration to maintain the 1:1 Sn/Se stoichiometry). On the basis of the data in Figure 4, several observations can be made. First, the transparency of the nanosheets with respect to the electron beam increases systematically with a decreasing amount of $SnCl_2$. While this is a qualitative observation, it suggests that the nanosheets are becoming thinner with decreasing $SnCl_2$ concentration. Consistent with this, the thinner nanosheets show a greater tendency to buckle and fold (Supporting Information, Figure S2). Second, representative AFM images and their corresponding line scan profiles provide a more quantitative measure of the systematic decrease in average nanosheet thickness: ~35 nm when 40 mg of $SnCl_2$ is used (Figure 4a), ~25 nm for 20 mg of $SnCl_2$ (Figure 4b), ~17 nm for 15 mg of $SnCl_2$ (Figure 4c), and ~8 nm for 10 mg of $SnCl_2$ (Figure 4d).

Powder XRD data help further characterize the nanosheet morphology and the systematic variation in average nanosheet thickness, as well as confirm that these features are representative of the bulk sample. As shown in Figure 5a, near-perfect preferred orientation is observed for drop-cast films of each sample. In addition to indicating the relative phase purity of the samples, the XRD data in Figure 5a confirm that the two-dimensional nanosheet morphology is maintained in the bulk sample upon reduction of thickness. Importantly, Figure 5b shows an overlay of the (400) peaks for the four samples synthesized using 40, 20, 15, and 10 mg of $SnCl_2$. (The powder XRD patterns were acquired using the same scan rate, dwell time, and step size, and the signal-to-noise ratio of the background is identical for all samples.) Comparing the full width at half-maximum for each of the peaks, increased peak broadening as a function of decreasing $SnCl_2$ reagent concentration is evident, and this is consistent with decreasing average nanosheet thickness as the amount of $SnCl_2$ is decreased. The nanosheet thicknesses as determined by Scherrer analysis of the (400) reflection were 32, 27, 23, and 17 nm for the samples prepared using 40, 20, 15, and 10 mg of $SnCl_2$, respectively. While the numbers do not exactly match those observed by AFM, the trends are the same, the values are comparable, and the XRD data are able to confirm a decrease in average nanosheet thickness with reduced reagent concentration for the entire bulk sample. Taken together, the AFM, TEM, and XRD data convincingly indicate a systematic decrease in nanosheet thickness that is tunable with Sn and Se reagent concentration, which occurs while maintaining the nanosheet morphology and good lateral uniformity.

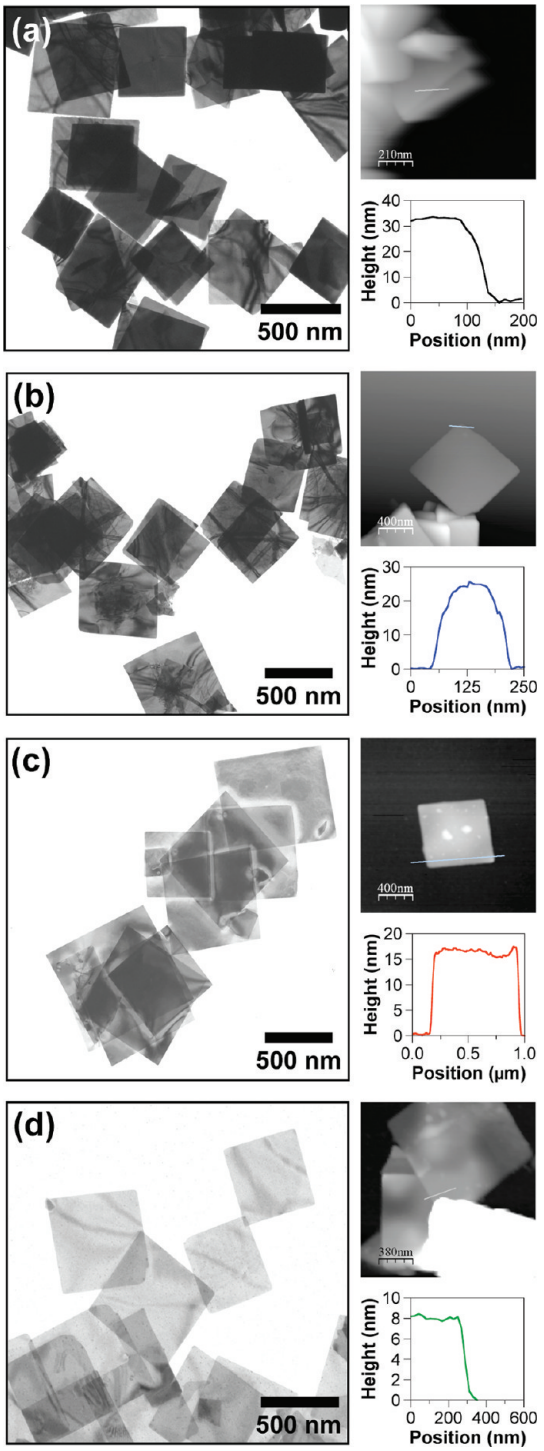


**Figure 4. TEM (left panels) and AFM (right panels) characterization of thickness tunability in the colloidal SnSe nanosheets, corresponding to samples prepared using (a) 40, (b) 20, (c) 15, and (d) 10 mg of $SnCl_2$. The line profiles, corresponding to the lines indicated in the AFM images, highlight the progressive reduction in sheet thickness as a function of the amount of $SnCl_2$ used in the reaction. The image in panel d includes a group of stacked nanosheets, which appears white because its height is taller than that of the maximum *z*-axis scale.**

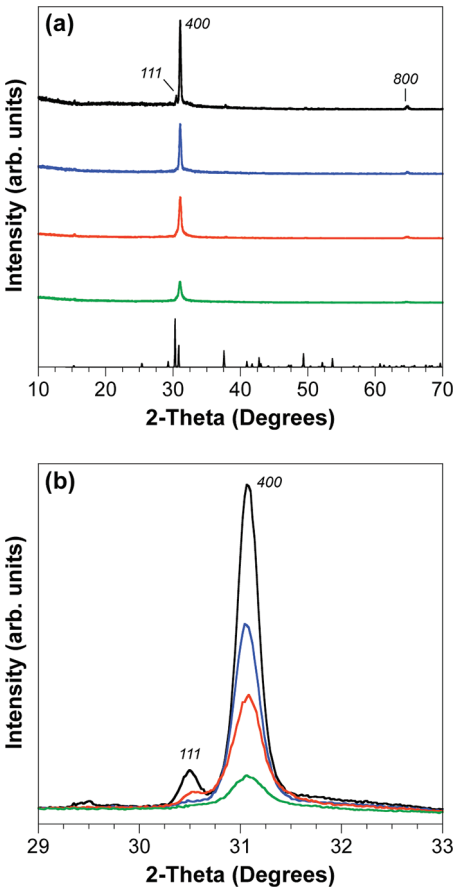


**Figure 5. Panel a shows powder XRD patterns for drop-cast films of the SnSe nanosheets, and panel b shows an overlay of the (400) peak to highlight the increased peak broadening as the nanosheet thickness decreases. The 40, 20, 15, and 10 mg samples are shown as black, blue, red, and green patterns (ordered from top to bottom with decreasing sheet thickness), respectively.**

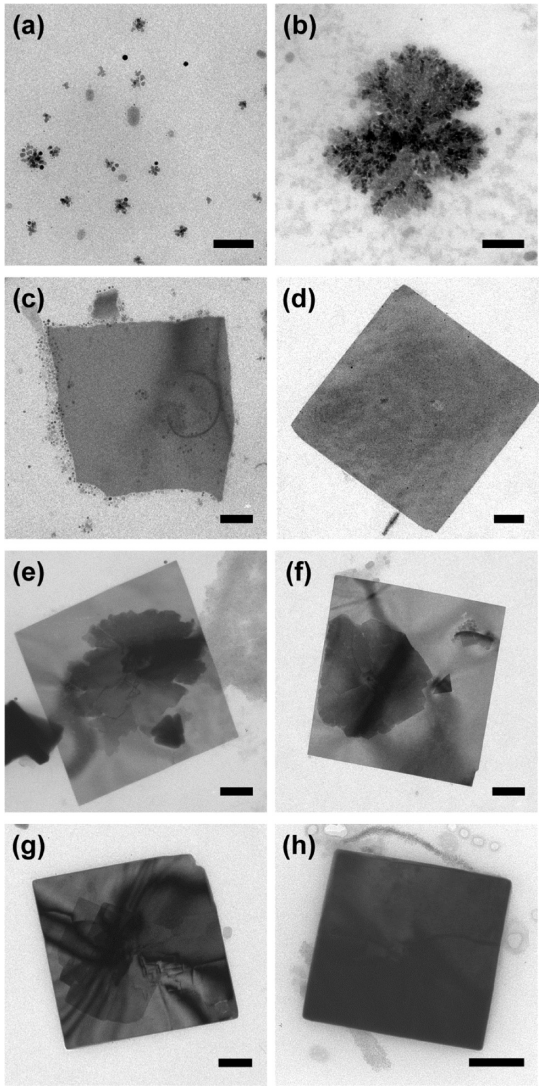


**Figure 6. TEM images of aliquots taken during the formation of the SnSe nanosheets, highlighting (a,b) initial nucleation, agglomeration, and coalescence of nanoparticle seeds into two-dimensional dendritic nanostructures, (c,d) lateral growth *via* nanoparticle attachment resulting in a uniform square-like nanosheet morphology, and (e–h) layer-by-layer vertical growth that produces a final single-crystalline nanosheet. Scale bars are 100 nm.**

**Nanosheet Formation Pathway.** TEM analysis of aliquots taken during the course of a reaction helps us to understand how the nanosheets form and why their thicknesses can be tuned based on reagent concentration. Figure 6 shows TEM snapshots of nanosheet formation at various stages of growth. In the earliest stage (Figure 6a), individual nanoparticle seeds are observed, along with small aggregates that each contain an average of 5–15 particles. These small nanoparticle aggregates appear to coalesce and grow into two-dimensional dendritic structures (Figure 6b). Further growth, predominantly in two dimensions, shows the continued addition of primary particles (Figure 6c), followed by the formation of the uniform square-like nanosheet structures that are observed as the primary products (Figure 6d). Interestingly, once lateral growth has defined the square-like nanosheet morphology, we see evidence of vertical growth that generally maintains the lateral dimensions while increasing the thickness (Figure 6e–h). Lateral growth appears to continue on the surface of the preformed nanosheets (Figure 6e–g), mimicking the initial stages of two-dimensional (2D) growth observed in Figure 6a, b. Apparently, the initial 2D nanostructure acts as a template for the growth of subsequent layers, which suggests that the nanosheets "grow out" laterally and then "grow up" vertically.

HRTEM studies provide further insights into the nanosheet growth process (Figure 7). In the early stages of growth, analogous to that shown in Figure 6b, a representative HRTEM image shows crystalline SnSe nanoparticles of approximately 2–4 nm in diameter that are agglomerated and fused together into an irregularly shaped 2D structure (Figure 7a). The orientations of the constituent particles appear random (as confirmed by the fast Fourier transform (FFT) image shown in Supporting Information, Figure S3), indicating

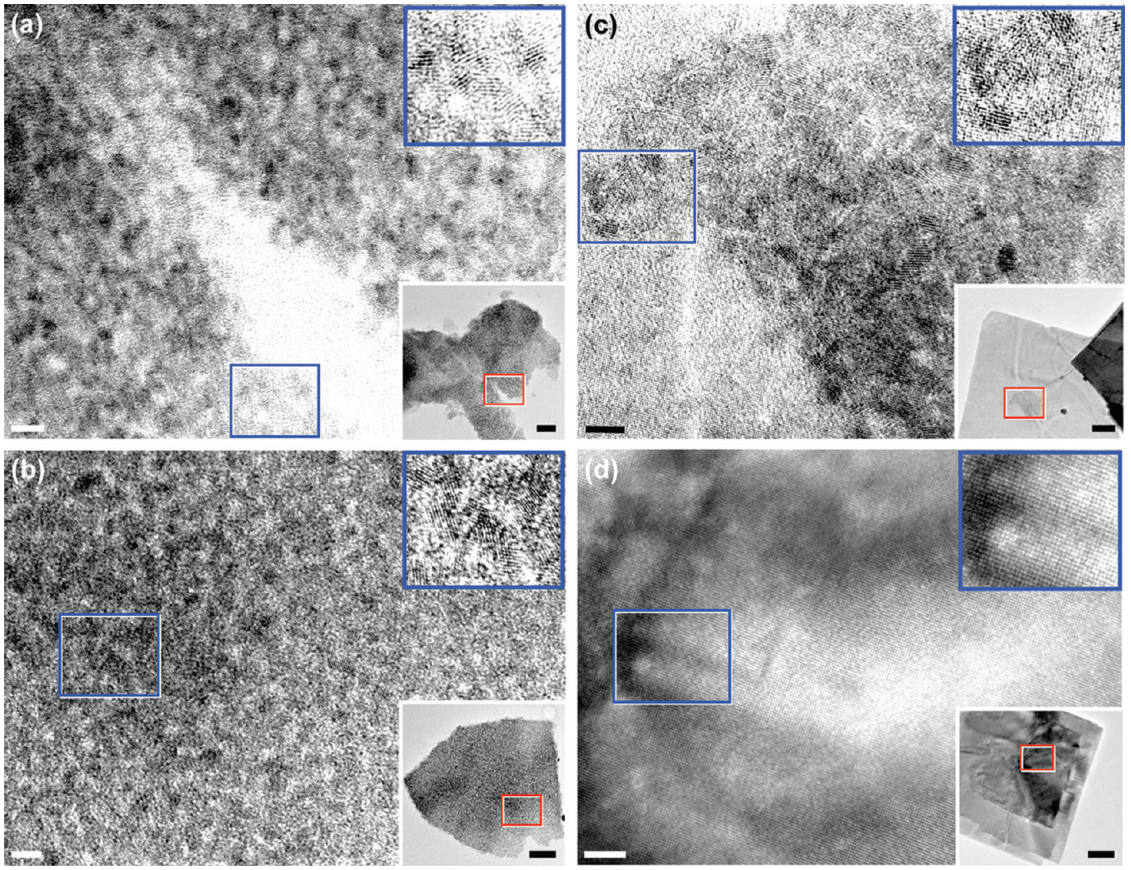


**Figure 7. HRTEM images highlighting the SnSe nanosheets at different stages of growth: (a,b) initial growth stages showing the attachment of randomly oriented nanoparticle building blocks, (c) epitaxial alignment of nanoparticle seeds on a preformed crystalline nanosheet template and subsequent growth *via* nanoparticle attachment, and (d) single-crystal nanosheet in the final stage of growth. Scale bars for main panel images (high-magnification) are 5 nm. Scale bars for images located in the insets (low-magnification) are 50 nm. The red boxes in each bottom-right inset correspond to the enlarged regions shown in the main panels. The blue boxes in each main panel correspond to the enlarged regions shown in the upper-right insets.**

that a polycrystalline 2D nanostructure forms first, followed by a transition to a single-crystal nanosheet. This is analogous to the formation pathway recently proposed for nanosheets of ceria,[40] which involved the sintering and reorientation of a polycrystalline $CeO_2$ nanosheet initially formed *via* nanoparticle aggregation, and is also related to the formation of free-standing CdTe nanosheets by the self-assembly of CdTe nanocrystals in solution.[38] As the nanosheet continues to grow, additional nanoparticle attachment occurs, and while the nanosheet remains polycrystalline (Supporting Information, Figure S4), larger domains of oriented particles are beginning to form (Figure 7b).

Figure 7c shows a representative HRTEM image of a fully formed SnSe nanosheet with evidence of nanoparticles beginning to attach to the nanosheet surface to facilitate vertical growth. Two observations are particularly important. First, the fully formed nanosheet (the "background") is now single-crystalline, as evidenced by the coherence of the lattice fringes across the entire nanosheet (Supporting Information, Figure S5). Apparently, the constituent nanoparticles of the polycrystalline nanosheet have coalesced and recrystallized to form a single crystal nanosheet. The lattice spacings ($d = 3.0$ Å) match well with the {011} set of planes in the SnSe crystal structure, which is consistent with the [100] nanosheet orientation observed earlier by XRD and TEM. Second, the nanoparticles that attach to the nanosheet surface show a preference for epitaxial alignment (Figure 7c), suggesting that oriented attachment may be involved in vertical growth.[41,63] This is consistent with the data presented in Figure 6, which suggested that vertical growth commences primarily after lateral growth is complete. Once lateral and vertical growth is complete, a single crystal nanosheet of SnSe is formed (Figure 7d and Supporting Information, Figure S6).

Collectively, the HRTEM data provide important insights into how the single crystal SnSe nanosheets form. Initially, individual SnSe nanoparticles nucleate, aggregate, and coalesce to form thin two-dimensional single crystal nanosheets *via* a polycrystalline nanosheet intermediate (Figure 6a-d). While some additional lateral growth is likely to occur, vertical growth becomes predominant, possibly *via* the oriented attachment of nanoparticles to the nanosheet surface

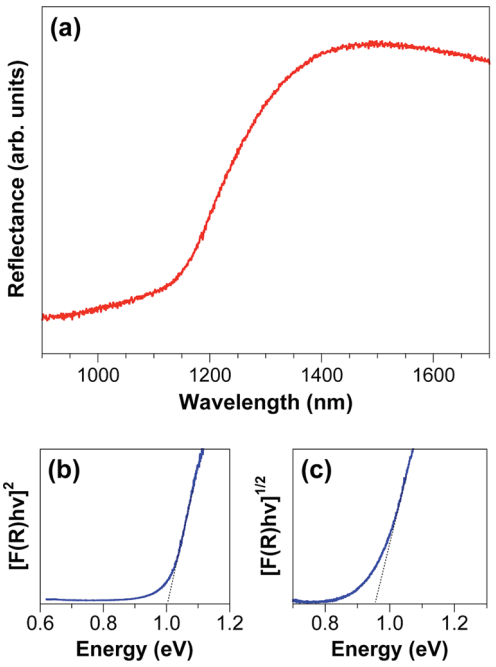


**Figure 8. (a) Diffuse reflectance spectrum for SnSe nanosheets. Direct and indirect bandgaps were determined from plots of $[F(R)h\nu]^2$ and $[F(R)h\nu]^{1/2}$ *vs* energy, shown in panels b and c, respectively.**

through epitaxial alignment (Figure 7c). This vertical growth continues, in a pseudo layer-by-layer fashion, until all of the available SnSe feedstock is consumed (Figure 6e–h). Thus, when lower concentrations of $SnCl_2$ and TOP-Se are used, fewer SnSe layers form, and vertical growth stops sooner due to a limited supply of the SnSe feedstock. Therefore, thicker nanosheets will result from higher reagent concentrations and thinner nanosheets will result from lower reagent concentrations (Figures 4 and 5). The factors that influence the lateral dimensions are not yet fully understood. However, they appear to be largely independent of reagent concentration and more closely correlated with the variables that influence initial growth, for example, reaction temperature and the organic/molecular species present. This is similar to the factors that have been identified to influence the lateral growth of smaller CdSe nanosheets.[32]

**Optical Properties of SnSe Nanosheets.** Diffuse reflectance data (Figure 8) were obtained from drop-cast films of the SnSe nanosheets on a glass substrate (Supporting Information, Figure S7). The onset of absorption was found to be in the near-infrared region at approximately 1350 nm.[51] To determine the indirect and direct bandgap values, Kubelka–Munk transformations were performed.[64] A plot of $[F(R)h\nu]^2$ *versus* energy indicates a direct bandgap of ~1 eV (Figure 8b), and a plot of $[F(R)h\nu]^{1/2}$ *versus* energy indicates an indirect bandgap of ~0.90 eV (Figure 8c). Both of these values are consistent with previous studies of the direct and indirect bandgap energies for SnSe.[46,51,52] Although not optimized, a film of SnSe nanosheets on FTO (which consists of the as-synthesized nanosheets that contain long-chain alkylamine stabilizers on their surfaces) showed a clear photoswitching response under light and dark conditions. These results indicate that drop-cast films of the SnSe nanosheets are photoactive with bandgaps that may make them appropriate, with further optimization, for potential applications in near-IR optoelectronic devices including multijunction solar cells,[45,48,52] radiation detectors,[53,65] and electrical and memory switching devices.[54]

## CONCLUSIONS

Two-dimensional colloidal nanosheets of SnSe have been made using a simple one-pot solution chemistry reaction. TEM studies reveal that the nanosheets adopt a square-like morphology with uniform lateral dimensions on the order of ~500 nm × 500 nm. TEM, AFM, and XRD studies collectively confirm that the nanosheet thickness can be tuned from approximately 10 to 40 nm, and this is accomplished while maintaining the nanosheet morphology and lateral uniformity. Importantly, studies of the nanosheet formation pathway suggest that lateral growth occurs first, followed by subsequent growth in the vertical direction. Therefore, when the reaction mixture had a limited amount of available Sn and Se reagents (*e.g.*, at lower reagent concentrations), growth in the vertical direction was limited and thinner nanosheets were formed. These insights into how the nanosheets form offer important clues for precisely controlling and tuning colloidal nanosheet thicknesses while maintaining lateral uniformity. While demonstrated for SnSe, these insights may have important implications for other technologically relevant oxide and chalcogenide semiconductor systems, helping to guide efforts in the synthesis and optimization of nanosheets with controlled dimensions for applications that include photocatalysis, photovoltaics, and field-effect transistors.[60,65–67]

## MATERIALS AND METHODS

**Materials.** Tin(II) chloride ($SnCl_2$, 99%) and selenium powder (99+%) were purchased from Alfa Aesar, oleylamine (>40%) was purchased from TCI America, and tri-*n*-octylphosphine (TOP, 90% tech.) and hexamethyldisilazane (HMDS, >99%) were purchased from Aldrich. Oleylamine and tri-*n*-octylphosphine were degassed prior to their use, and all other chemicals were used as received. All syntheses were carried out under Ar using standard Schlenk techniques, and workup procedures were performed in air.

**Characterization.** Powder XRD data were collected using a Bruker D8 Advance X-ray diffractometer equipped with Cu Kα radiation. TEM images and SAED patterns were obtained using a JEOL 1200 EX II TEM operating at 80 kV. HRTEM imaging and EDS analyses were performed on a JEOL-2010 $LaB_6$ TEM microscope operating at 200 kV. Samples were prepared by suspending the washed crystallites in toluene and drop-casting onto Formvar-coated copper TEM grids. Reflectance measurements were collected on a Perkin-Elmer Lambda 950 spectrophotometer equipped with a 150 mm integrating sphere. Samples were prepared by drop-casting a concentrated solution of the sheets onto a glass substrate to form a thick film. Scanning electron microscope (SEM) images were collected using a JEOL JSM 5400 SEM. Atomic force microscope (AFM) images were collected using a Dimension Instruments 3100 AFM equipped with PPP-NCHR tapping mode AFM tips from Nanosensors.

**Synthesis.** A 1 M TOP-Se stock solution was prepared by dissolving 790 mg (10 mmol) of selenium powder in 10 mL of TOP and sonicating until a clear colorless solution was obtained. In a typical synthesis of SnSe nanosheets, 40 mg (0.21 mmol) of $SnCl_2$ and 20 mL (~60 mmol) of oleylamine were added to a 20 mL scintillation vial and sonicated until a clear colorless solution was obtained. This solution was then added to a 3-neck round-bottom flask fitted with a condenser, thermometer adapter, thermometer, and rubber septum. Next, 0.22 mL of the 1 M TOP-Se stock solution and 1 mL (4.71 mmol) of hexamethyldisilazane (HMDS) were also added and stirred for 15 min. Finally, the solution was slowly heated to 240 °C at ~10 °C/min, resulting in the formation of a black-colored solution. This solution was allowed to age for 30 min and then was rapidly cooled by removing the reaction flask from the heating mantle. The samples prepared using 20, 15, and 10 mg of $SnCl_2$ were prepared using an identical procedure to the one above except that 0.11 mL, 0.080 mL, and 0.053 mL of the 1 M TOP-Se stock solution was used to give the appropriate 1:1 Sn/Se ratio, respectively. The SnSe nanosheets were precipitated by adding 30 mL of a 3:1:1 acetone/hexane/toluene mixture and then centrifuged at 12 000 rpm for 10 min. The obtained powder was washed three times with a 1:1 toluene/ethanol mixture with centrifugation in between each wash. The product could then be suspended in toluene, ethanol, or methanol for further characterization with dispersibility of the nanosheets lasting for approximately 10 min.

*Acknowledgment.* This work was supported primarily by the U.S. Department of Energy, Office of Basic Energy Sciences, Division of Materials Sciences and Engineering, under Award No. DE-FG02-08ER46483 (R.E.S., materials synthesis and characterization). D.D.V. acknowledges support from an NSF Graduate Research Fellowship. S.I.I. (photoelectrochemical measurements) was supported by a Research Corporation Scialog Award. TEM imaging was performed in the Electron Microscopy Facility of the Huck Institutes of the Life Sciences and in the Materials Characterization Facility at the Penn State Materials Research Institute. The authors acknowledge use of facilitates at the PSU site of the NSF NNIN. The authors thank Tad Daniels and Josh Stapleton at the Penn State Materials Characterization Laboratory for help with the AFM and diffuse reflectance measurements, respectively.

*Supporting Information Available:* Additional TEM, SEM, HRTEM, and FFT data. This material is available free of charge *via* the Internet at http://pubs.acs.org.

## REFERENCES AND NOTES

1. Coleman, J. N.; Lotya, M.; O'Neill, A.; Bergin, S. D.; King, P. J.; Khan, U.; Young, K.; Gaucher, A.; De, S.; Smith, R. J.; *et al.* Two-Dimensional Nanosheets Produced by Liquid Exfoliation of Layered Materials. *Science* **2011**, *331*, 568–571.
2. Ma, R. Z.; Sasaki, T. Nanosheets of Oxides and Hydroxides: Ultimate 2D Charge-Bearing Functional Crystallites. *Adv. Mater.* **2010**, *22*, 5082–5104.
3. Takagaki, A.; Tagusagawa, C.; Hayashi, S.; Hara, M.; Domen, K. Nanosheets as Highly Active Solid Acid Catalysts for Green Chemical Syntheses. *Energ. Environ. Sci.* **2010**, *3*, 82–93.
4. Mas-Balleste, R.; Gomez-Navarro, C.; Gomez-Herrero, J.; Zamora, F. 2D Materials: To Graphene and Beyond. *Nanoscale* **2011**, *3*, 20–30.
5. Wang, C.; Zhou, Y.; Ge, M. Y.; Xu, X. B.; Zhang, Z. L.; Jiang, J. Z. Large-Scale Synthesis of $SnO_2$ Nanosheets with High Lithium Storage Capacity. *J. Am. Chem. Soc.* **2010**, *132*, 46–47.
6. Compton, O. C.; Osterloh, F. E. Niobate Nanosheets as Catalysts for Photochemical Water Splitting into Hydrogen and Hydrogen Peroxide. *J. Phys. Chem. C* **2009**, *113*, 479–485.
7. Youngblood, W. J.; Lee, S. H. A.; Maeda, K.; Mallouk, T. E. Visible Light Water Splitting Using Dye-Sensitized Oxide Semiconductors. *Acc. Chem. Res.* **2009**, *42*, 1966–1973.
8. Takagaki, A.; Sugisawa, M.; Lu, D. L.; Kondo, J. N.; Hara, M.; Domen, K.; Hayashi, S. Exfoliated Nanosheets as a New Strong Solid Acid Catalyst. *J. Am. Chem. Soc.* **2003**, *125*, 5479–5485.
9. Hu, L. H.; Peng, Q.; Li, Y. D. Selective Synthesis of $Co_3O_4$ Nanocrystal with Different Shape and Crystal Plane Effect on Catalytic Property for Methane Combustion. *J. Am. Chem. Soc.* **2008**, *130*, 16136–16137.
10. Shah, D.; Maiti, P.; Gunn, E.; Schmidt, D. F.; Jiang, D. D.; Batt, C. A.; Giannelis, E. R. Dramatic Enhancements in Toughness of Polyvinylidene Fluoride Nanocomposites *via* Nanoclay-Directed Crystal Structure and Morphology. *Adv. Mater.* **2004**, *16*, 1173–1177.
11. Podsiadlo, P.; Kaushik, A. K.; Arruda, E. M.; Waas, A. M.; Shim, B. S.; Xu, J. D.; Nandivada, H.; Pumplin, B. G.; Lahann, J.; Ramamoorthy, A.; *et al.* Ultrastrong and Stiff Layered Polymer Nanocomposites. *Science* **2007**, *318*, 80–83.
12. Osterloh, F. E. Solution Self-Assembly of Magnetic Light Modulators from Exfoliated Perovskite and Magnetite Nanoparticles. *J. Am. Chem. Soc.* **2002**, *124*, 6248–6249.
13. Kim, J. Y.; Osterloh, F. E.; Hiramatsu, H.; Dumas, R. K.; Liu, K. Synthesis and Real-Time Magnetic Manipulation of a Biaxial Superparamagnetic Colloid. *J. Phys. Chem. B* **2005**, *109*, 11151–11157.
14. Hoertz, P. G.; Mallouk, T. E. Light-to-Chemical Energy Conversion in Lamellar Solids and Thin Films. *Inorg. Chem.* **2005**, *44*, 6828–6840.
15. Compton, O. C.; Mullet, C. H.; Chiang, S.; Osterloh, F. E. A Building Block Approach to Photochemical Water-Splitting Catalysts Based on Layered Niobate Nanosheets. *J. Phys. Chem. C* **2008**, *112*, 6202–6208.
16. Rao, C. N. R.; Sood, A. K.; Subrahmanyam, K. S.; Govindaraj, A. Graphene: The New Two-Dimensional Nanomaterial. *Angew. Chem., Int. Ed.* **2009**, *48*, 7752–7777.
17. Lee, K. Y.; Lim, J. R.; Rho, H.; Choi, Y. J.; Choi, K. J.; Park, J. G. Evolution of Optical Phonons in CdS Nanowires, Nanobelts, and Nanosheets. *Appl. Phys. Lett.* **2007**, *91*, 201901.
18. Sasaki, T.; Watanabe, M. Semiconductor Nanosheet Crystallites of Quasi-$TiO_2$ and their Optical Properties. *J. Phys. Chem. B* **1997**, *101*, 10159–10161.
19. Allen, M. R.; Thibert, A.; Sabio, E. M.; Browning, N. D.; Larsen, D. S.; Osterloh, F. E. Evolution of Physical and Photocatalytic Properties in the Layered Titanates $A_2Ti_4O_9$ (A = K, H) and in Nanosheets Derived by Chemical Exfoliation. *Chem. Mater.* **2010**, *22*, 1220–1228.
20. Fukuda, K.; Akatsuka, K.; Ebina, Y.; Ma, R.; Takada, K.; Nakai, I.; Sasaki, T. Exfoliated Nanosheet Crystallite of Cesium Tungstate with 2D Pyrochlore Structure: Synthesis, Characterization, and Photochromic Properties. *ACS Nano* **2008**, *2*, 1689–1695.
21. Osada, M.; Sasaki, T. Exfoliated Oxide Nanosheets: New Solution to Nanoelectronics. *J. Mater. Chem.* **2009**, *19*, 2503–2511.
22. Osada, M.; Akatsuka, K.; Ebina, Y.; Funakubo, H.; Ono, K.; Takada, K.; Sasaki, T. Robust High-Kappa Response in Molecularly Thin Perovskite Nanosheets. *ACS Nano* **2010**, *4*, 5225–5232.
23. Sakai, N.; Ebina, Y.; Takada, K.; Sasaki, T. Electronic Band Structure of Titania Semiconductor Nanosheets Revealed

by Electrochemical and Photoelectrochemical Studies. *J. Am. Chem. Soc.* **2004**, *126*, 5851–5858.
24. Osada, M.; Ebina, Y.; Fukuda, K.; Ono, K.; Takada, K.; Yamaura, K.; Takayama-Muromachi, E.; Sasaki, T. Ferromagnetism in Two-Dimensional $Ti_{0.8}Co_{0.2}O_2$ Nanosheets. *Phys. Rev. B* **2006**, *73*, 153301.
25. Zhang, J.; Soon, J. M.; Loh, K. P.; Yin, J. H.; Ding, J.; Sullivian, M. B.; Wu, P. Magnetic Molybdenum Disulfide Nanosheet Films. *Nano Lett.* **2007**, *7*, 2370–2376.
26. Coronado, E.; Marti-Gastaldo, C.; Navarro-Moratalla, E.; Ribera, A.; Blundell, S. J.; Baker, P. J. Coexistence of Superconductivity and Magnetism by Chemical Design. *Nat. Chem.* **2010**, *2*, 1031–1036.
27. Yu, J. G.; Fan, J. J.; Lv, K. L. Anatase $TiO_2$ Nanosheets with Exposed (001) Facets: Improved Photoelectric Conversion Efficiency in Dye-Sensitized Solar Cells. *Nanoscale* **2010**, *2*, 2144–2149.
28. Reddy, M. V.; Yu, T.; Sow, C. H.; Shen, Z. X.; Lim, C. T.; Rao, G. V. S.; Chowdari, B. V. R. Alpha-$Fe_2O_3$ Nanoflakes as an Anode Material for Li-ion Batteries. *Adv. Funct. Mater.* **2007**, *17*, 2792–2799.
29. Seo, J. W.; Jang, J. T.; Park, S. W.; Kim, C. J.; Park, B. W.; Cheon, J. W. Two-Dimensional $SnS_2$ Nanoplates with Extraordinary High Discharge Capacity for Lithium Ion Batteries. *Adv. Mater.* **2008**, *20*, 4269–4273.
30. Tae, E. L.; Lee, K. E.; Jeong, J. S.; Yoon, K. B. Synthesis of Diamond-Shape Titanate Molecular Sheets with Different Sizes and Realization of Quantum Confinement Effect During Dimensionality Reduction from Two to Zero. *J. Am. Chem. Soc.* **2008**, *130*, 6534–6543.
31. Son, J. S.; Yu, J. H.; Kwon, S. G.; Lee, J.; Joo, J.; Hyeon, T. Colloidal Synthesis of Ultrathin Two-Dimensional Semiconductor Nanocrystals. *Adv. Mater.* **2011**, *23*, 3214–3219.
32. Li, Z.; Peng, X. G. Size/Shape-Controlled Synthesis of Colloidal CdSe Quantum Disks: Ligand and Temperature Effects. *J. Am. Chem. Soc.* **2011**, *133*, 6578–6586.
33. Oyler, K. D.; Ke, X. L.; Sines, I. T.; Schiffer, P.; Schaak, R. E. Chemical Synthesis of Two-Dimensional Iron Chalcogenide Nanosheets: FeSe, FeTe, Fe(Se, Te), and $FeTe_2$. *Chem. Mater.* **2009**, *21*, 3655–3661.
34. Jang, J. T.; Jeong, S.; Seo, J. W.; Kim, M. C.; Sim, E.; Oh, Y.; Nam, S.; Park, B.; Cheon, J. Ultrathin Zirconium Disulfide Nanodiscs. *J. Am. Chem. Soc.* **2011**, *133*, 7636–7639.
35. Huang, X.; Tang, S.; Mu, X.; Dai, Y.; Chen, G.; Zhou, Z.; Ruan, F.; Yang, Z.; Zheng, N. Freestanding Palladium Nanosheets with Plasmonic and Catalytic Properties. *Nat. Nanotechnol.* **2011**, *6*, 28–32.
36. Seo, J. W.; Jun, Y. W.; Park, S. W.; Nah, H.; Moon, T.; Park, B.; Kim, J. G.; Kim, Y. J.; Cheon, J. Two-Dimensional Nanosheet Crystals. *Angew. Chem., Int. Ed.* **2007**, *46*, 8828–8831.
37. Ithurria, S.; Bousquet, G.; Dubertret, B. Continuous Transition from 3D to 1D Confinement Observed During the Formation of CdSe Nanoplatelets. *J. Am. Chem. Soc.* **2011**, *133*, 3070–3077.
38. Tang, Z.; Zhang, Z.; Wang, Y.; Glotzer, S. C.; Kotov, N. A. Self-Assembly of CdTe Nanocrystals into Free-Floating Sheets. *Science* **2006**, *314*, 274–278.
39. Schliehe, C.; Juarez, B. H.; Pelletier, M.; Jander, S.; Greshnykh, D.; Nagel, M.; Meyer, A.; Foerster, S.; Kornowski, A.; Klinke, C.; Weller, H. Ultrathin PbS Sheets by Two-Dimensional Oriented Attachment. *Science* **2010**, *329*, 550–553.
40. Yu, T.; Lim, B.; Xia, Y. Aqueous-Phase Synthesis of Single-Crystal Ceria Nanosheets. *Angew. Chem., Int. Ed.* **2010**, *49*, 4484–4487.
41. Zhang, Q.; Liu, S. J.; Yu, S. H. Recent Advances in Oriented Attachment Growth and Synthesis of Functional Materials: Concept, Evidence, Mechanism, and Future. *J. Mater. Chem.* **2009**, *19*, 191–207.
42. Dalmaschio, C. J.; Ribeiro, C.; Leite, E. R. Impact of the Colloidal State on the Oriented Attachment Growth Mechanism. *Nanoscale* **2010**, *2*, 2336–2345.
43. Zhang, J.; Huang, F.; Lin, Z. Progress of Nanocrystalline Growth Kinetics Based on Oriented Attachment. *Nanoscale* **2010**, *2*, 18–34.
44. Makinistian, L.; Albanesi, E. A. On the Band Gap Location and Core Spectra of Orthorhombic IV–VI Compounds SnS and SnSe. *Phys. Status Solidi B* **2009**, *246*, 183–191.
45. Antunez, P. D.; Buckley, J. J.; Brutchey, R. L. Tin and Germanium Monochalcogenide IV–VI Semiconductor Nanocrystals for Use in Solar Cells. *Nanoscale* **2011**, *3*, 2399–2411.
46. Guillen, C.; Montero, J. Herrero, Characteristics of SnSe and $SnSe_2$ Thin Films Grown onto Polycrystalline $SnO_2$-Coated Glass Substrates. *J. Phys. Status Solidi A* **2011**, *208*, 679–683.
47. Bicer, M.; Sisman, I. Electrodeposition and Growth Mechanism of SnSe Thin Films. *Appl. Surf. Sci.* **2011**, *257*, 2944–2949.
48. Franzman, M. A.; Schlenker, C. W.; Thompson, M. E.; Brutchey, R. L. Solution-Phase Synthesis of SnSe Nanocrystals for Use in Solar Cells. *J. Am. Chem. Soc.* **2010**, *132*, 4060–4061.
49. Baumgardner, W. J.; Choi, J. J.; Lim, Y. F.; Hanrath, T. SnSe Nanocrystals: Synthesis, Structure, Optical Properties, and Surface Chemistry. *J. Am. Chem. Soc.* **2010**, *132*, 9519–9521.
50. Ning, J.; Xiao, G.; Jiang, T.; Wang, L.; Dai, Q.; Zou, B.; Liu, B.; Wei, Y.; Chen, G.; Zou, G. Shape and Size Controlled Synthesis and Properties of Colloidal IV–VI SnSe Nanocrystals. *CrystEngComm.* **2011**, *13*, 4161–4166.
51. Drozd, V. E.; Nikiforova, I. O.; Bogevolnov, V. B.; Yafyasov, A. M.; Filatova, E. O.; Papazoglou, D. ALD Synthesis of SnSe Layers and Nanostructures. *J. Phys. D Appl. Phys.* **2009**, *42*, 125306.
52. Sharon, M.; Basavaswaran, K. Photoelectrochemical Studies on P-SnSe Electrodes. *Sol. Cells* **1987**, *20*, 323–332.
53. Pejova, B.; Tanusevski, A. A Study of Photophysics, Photoelectrical Properties, and Photoconductivity Relaxation Dynamics in the Case of Nanocrystalline Tin(II) Selenide Thin Films. *J. Phys. Chem. C* **2008**, *112*, 3525–3537.
54. Chun, D.; Walser, R. M.; Bene, R. W.; Courtney, T. H. Polarity-Dependent Memory Switching in Devices with SnSe and $SnSe_2$ Crystals. *Appl. Phys. Lett.* **1974**, *24*, 479–481.
55. Hickey, S. G.; Waurisch, C.; Rellinghaus, B.; Eychmuller, A. Size and Shape Control of Colloidally Synthesized IV–VI Nanoparticulate Tin(II) Sulfide. *J. Am. Chem. Soc.* **2008**, *130*, 14978–14980.
56. Xu, Y.; Al-Salim, N.; Bumby, C. W.; Tilley, R. D. Synthesis of SnS Quantum Dots. *J. Am. Chem. Soc.* **2009**, *131*, 15990–15991.
57. Zhang, Y. J.; Lu, J.; Shen, S. L.; Xu, H. R.; Wang, Q. B. Ultralarge Single Crystal SnS Rectangular Nanosheets. *Chem. Commun.* **2011**, *47*, 5226–5228.
58. Vaughn, D. D., II; Patel, R. J.; Hickner, M. A.; Schaak, R. E. Single-Crystal Colloidal Nanosheets of GeS and GeSe. *J. Am. Chem. Soc.* **2010**, *132*, 15170–15172.
59. Yoon, S. M.; Song, H. J.; Choi, H. C. p-Type Semiconducting GeSe Combs by a Vaporization–Condensation–Recrystallization (VCR) Process. *Adv. Mater.* **2010**, *22*, 2164–2167.
60. Tang, J. A.; Sargent, E. H. Infrared Colloidal Quantum Dots for Photovoltaics: Fundamentals and Recent Progress. *Adv. Mater.* **2011**, *23*, 12–29.
61. Talapin, D. V.; Lee, J. S.; Kovalenko, M. V.; Shevchenko, E. V. Prospects of Colloidal Nanocrystals for Electronic and Optoelectronic Applications. *Chem. Rev.* **2010**, *110*, 389–458.
62. Okazaki, A.; Ueda, I. The Crystal Structure of Stannous Selenide SnSe. *J. Phys. Soc. Jpn.* **1956**, *11*, 470.
63. Yeadon, M.; Ghaly, M.; Yang, J. C.; Averback, R. S.; Gibson, J. M. "Contact Epitaxy" Observed in Supported Nanoparticles. *Appl. Phys. Lett.* **1998**, *73*, 3208–3210.
64. Hagfeldt, A.; Gratzel, M. Light-Induced Redox Reactions in Nanocrystalline Systems. *Chem. Rev.* **1995**, *95*, 49–68.
65. Konstantatos, G.; Sargent, E. H. Nanostructured Materials for Photon Detection. *Nat. Nanotechnol.* **2010**, *5*, 391–400.
66. Lin, Y. J.; Yuan, G. B.; Liu, R.; Zhou, S.; Sheehan, S. W.; Wang, D. W. Semiconductor Nanostructure-Based Photoelectrochemical Water Splitting: A Brief Review. *Chem. Phys. Lett.* **2011**, *507*, 209–215.
67. Radisavljevic, B.; Radenovic, A.; Brivio, J.; Giacometti, V.; Kis, A. Single-Layer $MoS_2$ Transistors. *Nat. Nanotechnol.* **2011**, *6*, 147–150.